Energies **2015**, *8*, 3578-3590; doi:10.3390/en8053578

OPEN ACCESS

energies

ISSN 1996-1073

www.mdpi.com/journal/energies

Article

Hydrogen Storage in Pristine and d10-Block Metal-Anchored Activated Carbon Made from Local Wastes

Mohamed F. Aly Aboud [1,2,*], Zeid A. ALOthman [3], Mohamed A. Habila [3], Claudia Zlotea [4], Michel Latroche [4] and Fermin Cuevas [4]

[1] Sustainable Energy Technologies Center, College of Engineering, King Saud University, P.O. Box 800, Riyadh 11421, Saudi Arabia

[2] Mining, Metallurgical and Petroleum Engineering Department, Faculty of Engineering, Al-Azhar University, Nasr City, Cairo 11371, Egypt

[3] Advanced Materials Research Chair, Chemistry Department, P.O. Box 2455, College of Science, King Saud University, Riyadh 11451, Saudi Arabia; E-Mails: zaothman@ksu.edu.sa (Z.A.A.); mhabila@ksu.edu.sa (M.A.H.)

[4] ICMPE/CNRS-UPEC, UMR 7182, 2-8 rue Henri Dunant, 94320 Thiais, France; E-Mails: zlotea@icmpe.cnrs.fr (C.Z.); latroche@icmpe.cnrs.fr (M.L.); cuevas@glvt-cnrs.fr (F.C.)

* Author to whom correspondence should be addressed; E-Mail: aly@temple.edu or maboud@ksu.edu.sa; Tel.: +966-1-1467-6832; Fax: +966-1-1469-7122.

External Editor: Craig M. Jensen

Received: 18 November 2014 / Accepted: 20 April 2015 / Published: 28 April 2015

Abstract: Activated carbon has been synthesized from local palm shell, cardboard and plastics municipal waste in the Kingdom of Saudi Arabia. It exhibits a surface area of 930 m^2/g and total pore volume of 0.42 cm^3/g. This pristine activated carbon has been further anchored with nickel, palladium and platinum metal particles by ultrasound-assisted impregnation. Deposition of nanosized Pt particles as small as 3 nm has been achieved, while for Ni and Pd their size reaches 100 nm. The solid-gas hydrogenation properties of the pristine and metal-anchored activated carbon have been determined. The pristine material exhibits a reversible hydrogen storage capacity of 2.3 wt% at 77 K and 3 MPa which is higher than for the doped ones. In these materials, the spillover effect due to metal doping is of minor importance in enhancing the hydrogen uptake compared with the counter-effect of the additional mass of the metal particles and pore blocking on the carbon surface.

Keywords: activated carbon; hydrogen storage; spillover effect

1. Introduction

Hydrogen has become a promising substitute for fossil fuels in automotive applications due to its abundance and its higher chemical energy. Hydrogen holds three times the specific energy of gasoline [1]. Besides, it is environmentally friendly since its only oxidation product is water [2]. Owing to its extremely low density, a lot of efforts are in progress to reversibly store hydrogen by different methods. The main avenues can be summarized in two groups. The first avenue is chemical storage where chemical bonds occur between hydrogen atoms and receptors to form hydride phases [3,4]. Some of these materials are heavy, expensive and difficult to regenerate on-board. Additionally the thermodynamic stability of these compounds is usually high and a lot of energy is needed for releasing the hydrogen back during the desorption process. The second avenue is physical storage where hydrogen is kept in its molecular state. Physical storage can be performed in three ways:

i) Liquefaction of hydrogen, which requires cryogenic temperatures and efficient insulation. This wastes around 30% of the available energy from burning the hydrogen which makes this storage method a costly process [5].

ii) Compression of hydrogen gas in high-pressure tanks raises safety concern issues mainly as results of hydrogen embrittlement effects. Additionally the low gravimetric storage should also be considered if we include the mass of the tank [6].

iii) Physisorption in porous materials, which attracts scientific interests due to its simplicity. The large surface areas of porous materials, especially of nanostructures, allow the adsorption of large quantities of hydrogen.

Activated carbon (AC) is among the potential candidates for the last route because of its abundance, low cost, non-toxicity, good chemical stability, low density, good recycling characteristics and wide range of pore structures and forms [7–12]. The main factor that limits the storage of hydrogen on the carbon surface is the low energy of adsorption, in the range of 4–8 kJ/mol H_2 for most porous carbons.

Metal atom decoration on graphitic skeletons can increase the hydrogen uptake by introducing strong hydrogen interaction sites on the carbonaceous surfaces. Besides, these metallic centers facilitate the dissociation of hydrogen molecules and eventually increase the hydrogen content over the carbon receptor by a spillover mechanism [13].

In this work, high surface area activated carbon was produced from local wastes and decorated with some d^{10}-block transition elements (Ni, Pd and Pt). Park *et al.* reported that the amount of hydrogen storage capacity for Multi Walled Carbon Nanotubes (MWCNTs) increased in proportion to the Pt content with an optimum loading value of 4 wt% [14]. Zubizarreta *et al.* reported that the optimum nickel content for improving the hydrogen storage in carbon nanospheres was 5 wt% [15], while, Kim *et al.* found that hydrogen storage increased up to 1.23 wt% after loading with 8 wt% of nickel nanoparticles due to the spillover effect [16]. For Pd doping, Lueking *et al.* reported that the optimum loading for hydrogen storage on activated carbon is 14 wt%, while it is 5.7 wt% in single wall carbon

nanotubes [17]. Mu *et al.* used 20 wt% of palladium for enhancing the hydrogen storage capacity in etched carbon nanotubes [18].

After performing detailed chemical, structural and thermal characterizations, the hydrogen storage properties of the metal-anchored activated carbons were determined and compared to those of the pristine material.

2. Results and Discussion

2.1. Structural, Chemical and Thermal Characterizations

Figure 1 displays the X-Ray Diffraction (XRD) patterns of all studied samples. For the pristine activated carbon almost no diffraction peaks are detected due to its poor crystallinity. However, a tiny peak around 2θ° = 26.5° might correspond to the (002) plane of graphite [19]. After Pt-anchoring, an additional and very broad peak is detected at 2θ = 39.7°. It is assigned to the diffraction plane (111) of the *fcc* structure of Pt according to JCPDS card No. 03-065-2868. This strong peak broadening is attributed to the ultra-small size of platinum particles, which will be later supported by High-Resolution Transmission Electron Microscope (HRTEM) analysis. For the Ni-anchored sample, well-defined diffraction peaks are detected at 44.5° (111), 52° (200) and 76.5° (220) in 2θ°. They are characteristic of *fcc* nickel in agreement with the JCPDS card No. 03-065-2865. Finally, for the Pd-anchored sample sharp diffraction peaks are detected at 2θ° of 39.88° (111), 46.45° (200), 67.96° (220), 82° (311) and 86° (222) showing the occurrence of *fcc* Palladium (JCPDS card No. 03-065-2867).

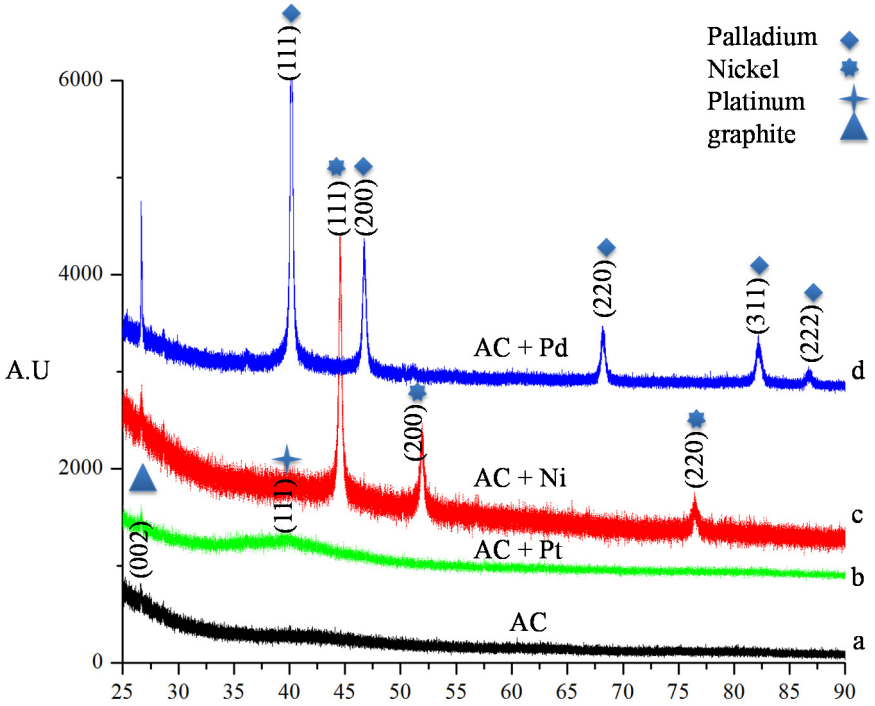

Figure 1. XRD diffraction patterns of (**a**) activated carbon (AC), (**b**) Pt-anchored AC, (**c**) Ni-anchored AC and (**d**) Pd-anchored AC.

Backscattered SEM images for pristine activated carbon AC, Pt-, Ni- and Pd-anchored AC are shown in Figure 2a to 2d, respectively. The pristine AC exhibits a fibrous layer structure with particle

dimensions of ~30 μm in length and ~4 μm in thickness. Cavities and porosity are observed as result of the evaporation of the activating agent. Both Ni- and Pd-anchored particles have spherical morphology with particle size ~100 nm. Nickel particles are uniformly dispersed over the AC, while Pd particles tend to agglomerate. SEM images failed to detect the presence of platinum particles on the surface of the activated carbon (Figure 2b) due to its low spatial resolution. Therefore, HRTEM investigations were used for Pt-AC as shown in Figure 3. The platinum particles are homogeneously distributed with ultra-small particle size of ~3 nm. The formation of such ultra-small particles of platinum compared to other anchored metals is consistent with the reported observation by Okhlopkova *et al.* that referred to the aggregation effect of palladium compared to platinum [20].

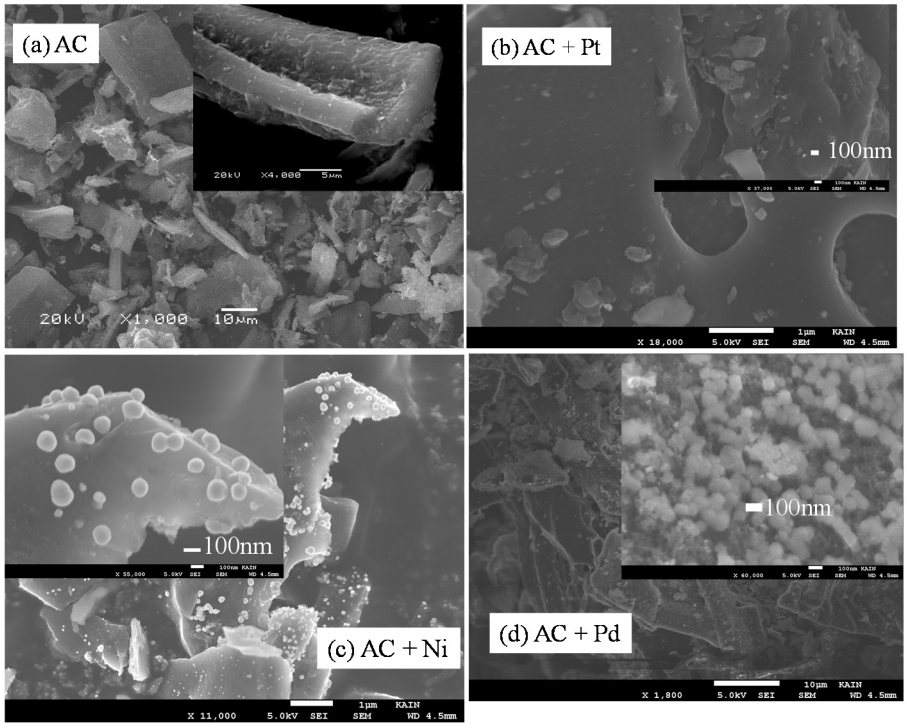

Figure 2. SEM images of (**a**) activated carbon (AC), (**b**) Pt-anchored AC, (**c**) Ni-anchored AC and (**d**) Pd-anchored AC.

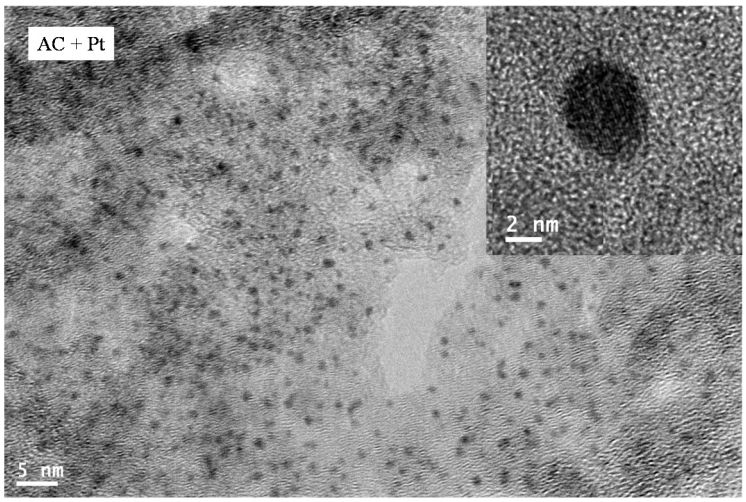

Figure 3. HRTEM images of Pt-anchored activated carbon.

The FTIR spectra recorded for all samples in the 400–4,000 cm^{-1} range are displayed in Figure 4. Almost no difference is seen between the activated carbon and the metal anchored activated carbons. The main groups are both alkene and aromatic C=C functions in addition to hydroxyl (OH^-) groups.

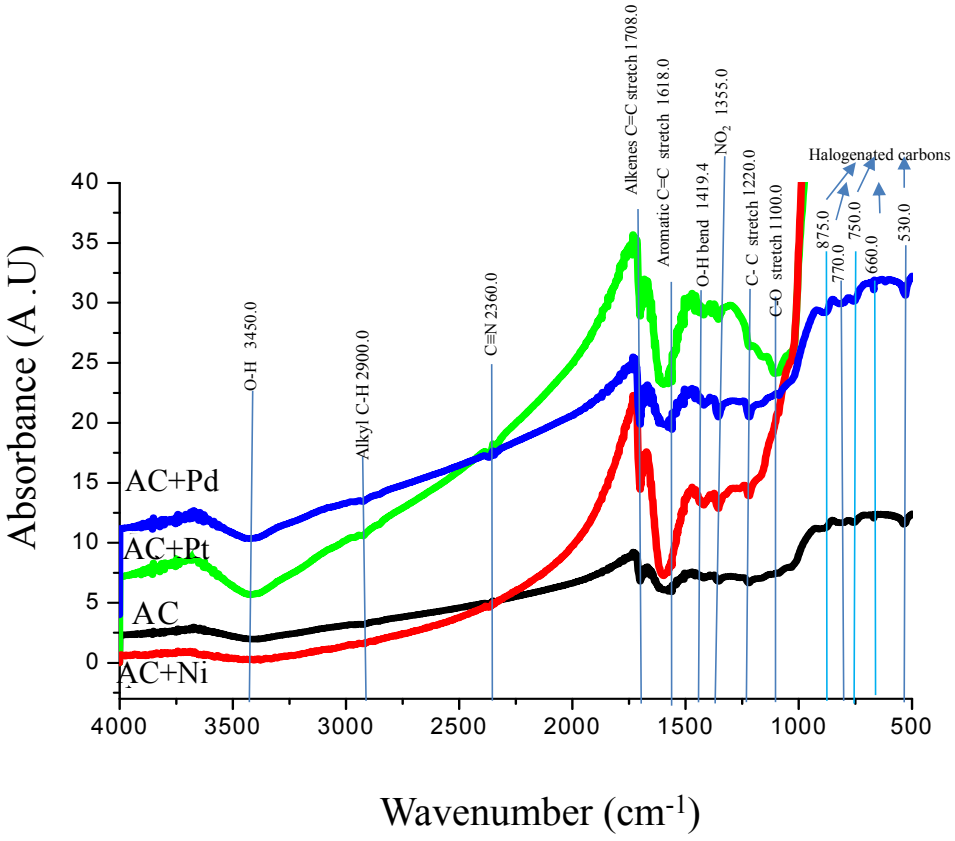

Figure 4. FTIR spectra for activated carbon (AC) and metal-anchored AC + Ni, AC + Pd and AC + Pt.

Figure 5 shows the monitored Differential Scanning Calorimetry (DSC) (Figure 5a) and Thermal Gravimetric Analysis (TGA) (Figure 5b) traces under air flow. For all samples, exothermic reactions due to carbon oxidation are observed. DSC peak temperatures are observed at ~820 K for both the AC and Ni-anchored materials, while they occur at ~770 K and 650 K for Pd- and Pt-anchored ones, respectively. The DSC onset reaction temperatures, as determined from the tangential method, are observed at ~675 K for AC, Ni- and Pd-anchored samples. Interestingly, the onset temperature for Pt-anchored AC is as low as 600 K. The lower oxidation temperature for the Pt containing sample is attributed to the ultra-fine Pt particles which enhance the oxidation reaction.

Figure 5b shows the TGA traces for all samples. Weight losses below 400 K are likely related to desorption of residual adsorbed moisture and volatile matter. Next, in agreement with the DSC analyses, release of CO_2 due to carbon oxidation takes place in the 600–873 K range leading to severe mass loss. Above this temperature range, no significant mass changes occur. The reported TGA curves allow estimating the actual metal doping of the different samples. It can be evaluated from the final weighted TGA mass considering that the amount of carbon ashes is constant for all samples (evaluated as *ca.* 9 wt% for pristine AC) and that the anchored metals form oxide species NiO, PdO, and PtO_2 by reaction with air. The thus-estimated metal doping is 6.5 wt% Ni, 16 wt% Pd, and 5 wt% Pt for nickel-, palladium- and platinum-anchored activated carbon samples, respectively.

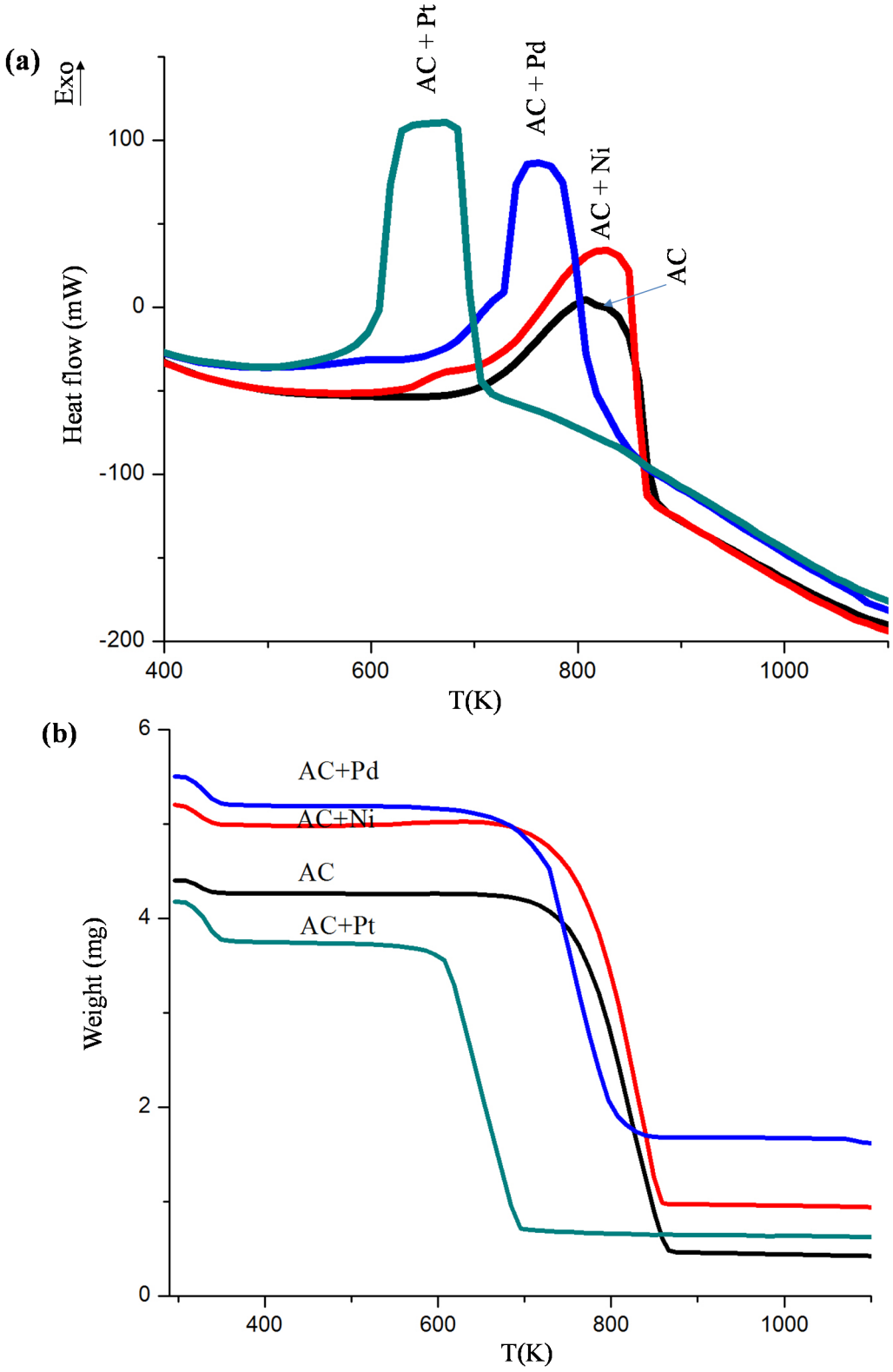

Figure 5. (**a**) DSC analysis under air flow of activated carbon (AC) and metal-anchored AC + Ni, AC + Pd and AC + Pt, and (**b**) TGA analysis under air flow of AC and metal-anchored AC + Ni, AC + Pd and AC + Pt.

2.2. Textural Characterization

Figure 6 shows the nitrogen adsorption isotherms at 77 K of pristine AC and Ni-, Pt-, Pd-anchored activated carbon. The isotherms are Type I, typical of microporous materials with a narrow pore size distribution. The textural properties are summarized in Table 1. The pristine AC as well as both Ni- and Pt-anchored samples have similar textural properties with Brunauer-Emmett-Teller (BET) surface area $A_s \sim 900$ m^2/g, total pore volume $V_{tot} = 0.42$ cm^3/g and micropore volume $V_\mu \sim 0.35$ cm^3/g. The Pd-anchored sample exhibits much lower textural properties.

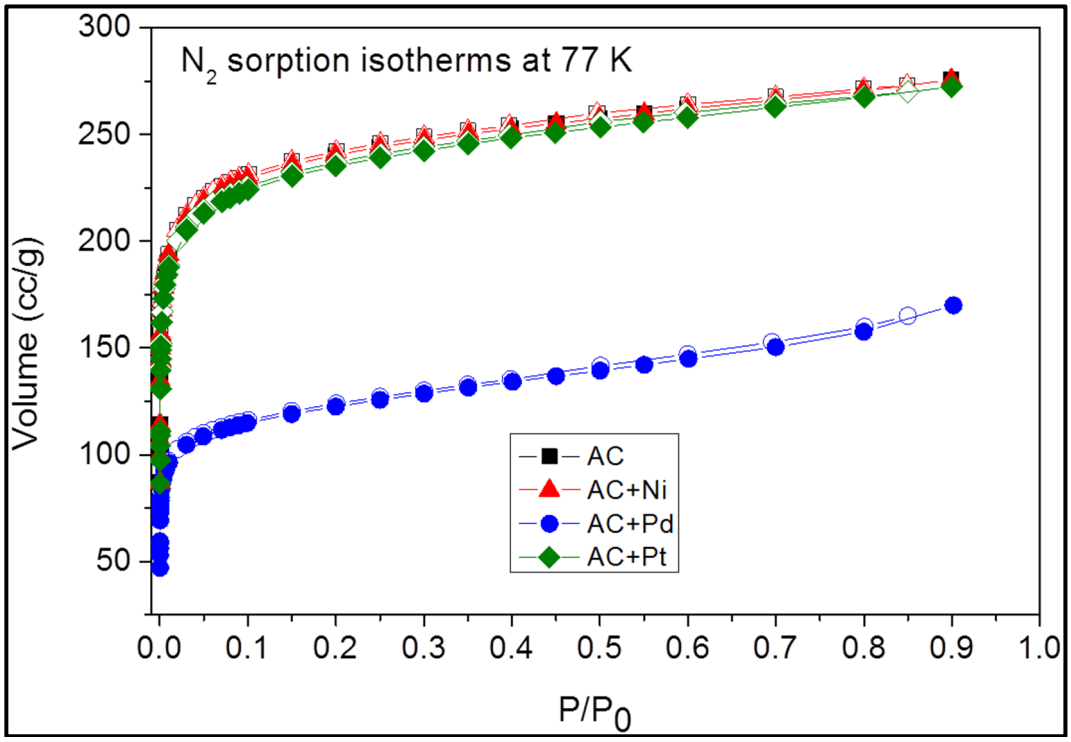

Figure 6. Nitrogen adsorption isotherms at 77 K of pristine and Ni-, Pd- and Pt-anchored activated carbon.

Table 1. Textural properties of pristine and Ni-, Pt-, Pd-anchored activated carbon.

Sample	Skeletal Density g/cm^3	A_s (BET) m^2/g	V_{tot} (P/P_0 = 0.9) cm^3/g	V_μ (DR) cm^3/g
Activated carbon	1.7 ± 0.1	931 ± 20	0.42 ± 0.1	0.36 ± 0.1
AC + Ni	1.9 ± 0.1	910 ± 20	0.42 ± 0.1	0.35 ± 0.1
AC + Pt	1.9 ± 0.1	889 ± 20	0.42 ± 0.1	0.34 ± 0.1
AC + Pd	2.0 ± 0.1	455 ± 20	0.26 ± 0.1	0.17 ± 0.1

Although the textural properties of activated carbons can vary depending on the processing techniques and precursors, the values reported here are almost identical to activated carbon made from Malaysian palm shells that were physically activated with steam (A_s = 941 m^2/g, V_{tot} = 0.52 cm^3/g) [21]. Moreover, they are much better than for H_3PO_4 chemically activated Malaysian palm (A_s = 615 m^2/g, V_{tot} = 0.28 cm^3/g) [22]. Also, the textural properties of our AC is superior to the activated carbon made from palm shells that underwent both chemical and physical treatments (A_s = 642 m^2/g, V_{tot} = 0.28 cm^3/g) [22].

The slight decrease for the surface area of the Ni- and Pt-anchored ACs compared with the pristine one is consistent with the reported data for Pt doped super-activated carbons [23]. This decrease was attributed to metal particles filling or blocking pores in the activated carbon. The drastic decrease for Pd-AC, with BET surface area about half that of Ni- and Pt-anchored AC, likely results from the high agglomeration of Pd-particles at the AC surface (Figure 2d).

The increase in the density of the metal anchored AC compared with the pristine one is due to the higher density of metal particles as compared to that of the adsorbent. Such an effect is consistent with the higher reported density of doped Pd-activated carbon fibers compared to non-doped ones [24]. The low surface area and pore volumes for palladium supported activated carbon due to agglomeration result in more packed and dense material compared to other doped activated carbons due its higher loading as was confirmed by the TGA measurements (Figure 5b).

2.3. Hydrogen Storage Measurements

Pressure Composition Isotherm (PCI) curves at 77 K and 298 K for all samples are shown in Figure 7 and the hydrogen uptake capacities are summarized in Table 2. In all cases, no hysteresis (below the experimental error) is observed, indicating that the adsorbed hydrogen can be desorbed reversibly when the pressure is released.

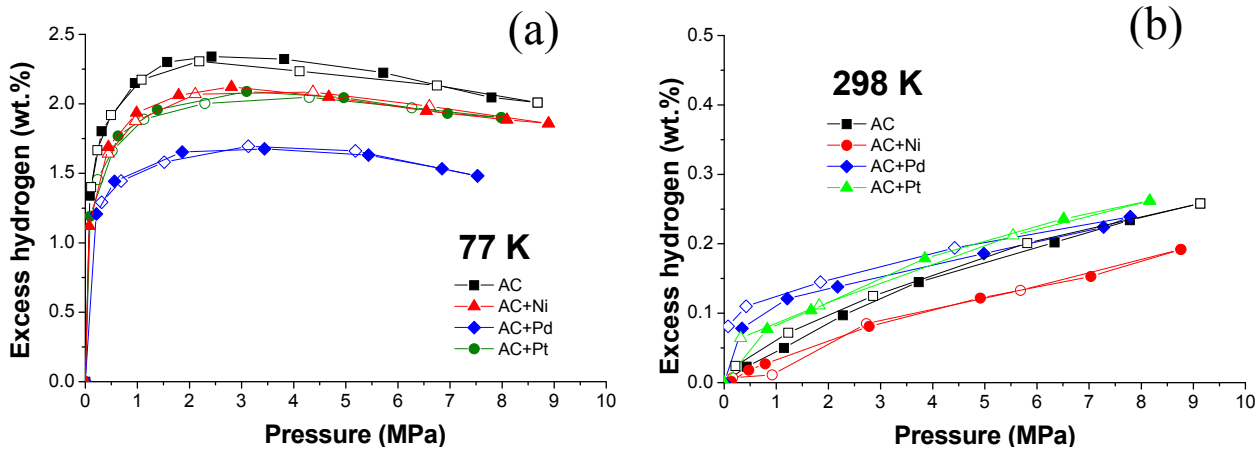

Figure 7. Pressure composition isotherm curves at (**a**) 77 K and (**b**) 298 K for the activated carbon (AC), Ni- , Pd- and Pt-anchored AC. Full and empty symbols stand for adsorption and desorption measurements, respectively.

All low temperature (77 K) the PCI curves exhibit Type I isotherms. This indicates monolayer adsorption of hydrogen molecules, which extent depends on the micropore volume and its filling. The hydrogen uptake increases up to 3 MPa and then reaches a maximum due to the completion of micropore filling. The amount of adsorbed hydrogen in the pristine activated carbon is consistent with the maximum theoretical capacity established by Ströbel *et al.* for carbonaceous materials [25]. These authors showed that the hydrogen uptake on carbon surface could be derived as:

$$H\,(\text{wt\%}) = 2.27 \times 10^{-3} \cdot A_s\,(\text{m}^2/\text{g}) \quad (1)$$

where A_s is the surface area of the carbonaceous material. Using Equation (1) and substituting for the observed surface area A_s = 931 m^2/g, we obtain a theoretical hydrogen uptake of 2.1 wt% in close

agreement with the reported value of 2.3 wt%. Moreover, these capacities are consistent with the reported data for wide range of carbon-based materials with wide textural properties [26–29]. The density of the adsorbed hydrogen at 77 K can be calculated from the hydrogen uptake (2.3 wt%) and the volume occupied by hydrogen in the micropore volume (0.36 cm^3/g). The calculated density equals 0.063 g/cm^3, lower than the reported density for liquid hydrogen at 20 K (0.071 g/cm^3) [30].

Table 2. Hydrogen uptake for pristine activated carbon and Ni-, Pt- and Pd-anchored activated carbon at 77 and 298 K.

Sample	H_2 Excess Capacity (wt%)	
	77 K at 3 MPa	298 K at 8 MPa
Activated carbon	2.3 ± 0.1	0.24 ± 0.01
AC + Ni	2.1 ± 0.1	0.17 ± 0.01
AC + Pt	2.1 ± 0.1	0.26 ± 0.01
AC + Pd	1.7 ± 0.1	0.25 ± 0.01

At 298 K and high-pressure (Figure 7b), both adsorption and desorption PCI isotherms exhibit linear behavior with low hydrogen uptake (≤0.26 wt%). Such a low capacity is attributed to the low enthalpy of hydrogen adsorption [31] and concurs with earlier reports on platinum doping in super activated carbon [18] and palladium in mesoporous carbon [32]. Similar capacities have been reported for hydrogen storage in activated carbon of even higher surface area A_s = 3,500 g/cm^3 [23]. At high pressure, pure AC, Pd- and Pt-anchored activated carbons exhibit rather similar hydrogen uptake, whereas Ni-anchored activated carbon has lower capacity. At room temperature and low pressure, Pd-anchored activated carbon has higher capacity than all other materials. This confirms the formation of palladium hydride at room temperature and low pressure, as demonstrated previously [28,29,32]. However, at high pressure, the favorable effect of palladium hydride formation is counteracted by the weight of the dopant, the filling of adsorbent micropores and pore blocking. These latter drawbacks could be counterbalanced if metal deposition would induce a significant hydrogen uptake by spillover effect. Unfortunately, the low hydrogen uptake at high pressure suggests that the spillover effect, if it exists, turns out to be of minor importance in the studied systems.

3. Experimental Section

Palm shell, cardboard and plastics collected from a municipal solid waste station in Riyadh, Saudi Arabia were used as raw material precursors in the present study. The mixing ratio was 1:1:0.33 by weight. The choice of such raw materials was given due to their abundance in the kingdom which will be in great advantage for a green environment. The elemental analysis for the raw materials and their activation process are given in [33,34]. The used metal precursors were nickel acetate tetrahydrate ($Ni(OCOCH_3)_2 \cdot 4H_2O$, 99%, E. Merck, darmstadt, Germany), palladium acetate ($Pd(OCOCH_3)_2$, 99%, Sigma Aldrich, St. Louis, MO, USA) and hexachloroplatenic acid ($H_2PtCl_6 \cdot XH_2O$, assay 40.0% Loba Chemie, Mumbai, India).

The ultrasound-assisted impregnation method was used to anchor metal particles on activated carbon surface because of its simplicity and its large scale [35–38]. Deionized water was used as dissolving media for both nickel acetate and platinum chloride while ultra-high purity benzene was used for dissolving palladium acetate. In the same dissolving media, activated carbon was dispersed using an

ultrasonic bath and mixed with the dissolved metal salt to nominally form a 10 wt% of anchored metal activated carbon. The mixture was left several days under the hood with repetitive stirring to achieve complete evaporation of the solvents. The resulted impregnated powders were grounded in ceramic mortar for homogenizing the impregnated materials. Same solvents were added to the resulted impregnated powders extra two times and followed by same procedure to ensure well dispersion. The resulted metal supported activated carbons were annealed at 523 K for 2 h under a continuous flow of hydrogen atmosphere to reduce the supported metal salts.

All samples underwent structural analysis by X-ray diffraction (XRD) using a X'Pert PRO Philips diffractometer (Eindhoven, The Netherlands), operated at 40 mA and 40 kV with CuK_{α} radiation and a nickel filter. Measurements were performed over the 2-theta range from 2° to 100° by steps of 0.02°, with a sampling time of one second per step. Sample morphology was investigated using a Field-Emission Scanning Electron Microscope (FE-SEM, model FEI-200NNL, Hillsboro, OR, USA) and a High-Resolution Transmission Electron Microscope (HRTEM, model JEM-2100F, JEOL, Tokyo, Japan). Surface chemistry was studied by Fourier Transform Infrared (FT-IR) transmission spectroscopy using a Nicolet 6700 FT-IR spectrophotometer (Thermo Scientific,Waltham, MA, USA). To this aim, samples were mixed with 98% wt% of KBr and then finely ground to make pellets. Thermal stability was investigated using a Differential Scanning Calorimetry–Thermal Gravimetric Analysis (TGA/DSC1 Star^{e}) system (Mettler Toledo, Columbus, OH, USA). TGA/DSC runs were performed under air within the temperature range 298–1,100 K with a heating rate of 5 K/min.

The textural properties were determined from nitrogen adsorption/desorption isotherms using an Autosorb-iQ Automated Gas Sorption Analyzer from Quantachrome Instruments (Hartley Wintney, UK). All isotherms have been measured by volumetric means. Samples were previously degassed overnight at 473 K. The specific surface area was obtained by the Brunauer-Emmett-Teller (BET) method. The total pore volume was computed from the amount of gas adsorbed at $P/P_0 = 0.9$, and the micropore volume was calculated using the Dubinin-Radushkevich (DR) equation.

Hydrogen sorption properties of samples were determined by measuring the Pressure-Composition-Isotherms (PCI) at 77 and 298 K up to 9 MPa hydrogen pressure. The PCI curves were recorded using a manual volumetric device (Sievert's method) equipped with calibrated and thermostated volumes and pressure gauges. The samples were enclosed in a stainless steel sample holder closed with a metal seal. Before any sorption measurements, the samples were degassed under secondary vacuum at 473 K for 12 h. Weight losses were measured as 3.1, 3.5, 6.8 and 5.6 wt% for non-doped, Ni-doped, Pt-doped and Pd-doped samples, respectively. The sample holder is immersed in a liquid nitrogen Dewar at 77 K or a thermostated water bath maintained at 298 K, and high purity hydrogen (6N) is introduced step by step up to 9 MPa. The pressure variations due to both gas expansion and hydrogen sorption are measured after reaching thermodynamic equilibrium, usually in the range of minutes. Real equation of state for hydrogen gas is used from the program GASPAK V3.32. The PCI curves were measured twice (*i.e.*, two full adsorption–desorption cycles) in order to check the hysteresis effect and the measurement repeatability. Good repeatability has been obtained for all samples. All capacities reported are excess hydrogen sorption quantities and refer to the sample dry mass (*i.e.*, degassed mass). Sample volume correction is derived from skeletal density measurements and data correspond to the excess values obtained by He pycnometry (Utrapyc 1200 Quantachrome, Hartley Wintney, UK).

4. Conclusions

Activated carbon was successfully synthesized from local palm shell and other wastes. The pristine activated carbon was impregnated with nickel, palladium and platinum. Coarse metallic nanoparticles of typical size 100 nm are formed for Ni- and Pd-anchored samples, whereas ultra-small particles size of 3 nm were obtained for the Pt case.

The hydrogen adsorption mechanism for all the synthesized samples occurs via micropore filling. No significant hysteresis was observed for any of the samples, indicating that adsorbed hydrogen can be desorbed reversibly when the pressure is released. At 298 K and 8 MPa both adsorption and desorption showed linear behavior with a low amount of hydrogen uptake. Low hydrogen uptake at ambient temperature is attributed to the low enthalpy of hydrogen adsorption on carbon surface.

At 77 K and 3 MPa, the activated carbon showed hydrogen storage of 2.3 wt% which is consistent with the BET surface area of ~931 m^2/g. Under the same conditions, metal-anchored activated carbons exhibited lower hydrogen uptakes ranging between 1.7 and 2.1 wt%. For the materials used in this study, possible spillover effects induced by the presence of metallic dopants are counterbalanced in terms of hydrogen storage by the concomitant addition of metal mass and reduction of carbon porosity.

Acknowledgments

The authors gratefully thank Sustainable Energy Technologies (SET) Center at King Saud University for financing this work.

Author Contributions

Mohamed F. Aly Aboud conceived and designed the experiments, performed the doping experiments and all data analysis; Mohamed F. Aly Aboud wrote the paper; Claudia Zlotea performed the textural characterization and hydrogen storage measurements; Claudia Zlotea, Michel Latroche and Fermin Cuevas participated in data analysis, paper writing and corrections; Zeid A. ALOthman and Mohamed A. Habila provided the virgin activated carbons and participated in FTIR analysis and provided important suggestions. All authors examined and approved the final manuscript.

Conflicts of Interest

The authors declare no conflict of interest.

References

1. Schlapbach, L.; Züttel, A. Hydrogen-storage materials for mobile applications. *Nature* **2001**, *414*, 353–358.
2. Rostrup-Nielsen, J.R.; Rostrup-Nielsen, T. Large-scale hydrogen production. *Cattech* **2002**, *6*, 150–159.
3. Krasae-In, S.; Stang, J.H.; Neksa, P. Simulation on a proposed large-scale liquid hydrogen plant using a multi-component refrigerant refrigeration system. *Int. J. Hydrog. Energy* **2010**, *35*, 4524–4533.
4. Barthélémy, H. Effects of pressure and purity on the hydrogen embrittlement of steels. *Int. J. Hydrog. Energy* **2011**, *36*, 2750–2758.

5. Kleperis, J.; Wójcik, G.; Czerwinski, A.; Skowronski, J.; Kopczyk, M.; Beltowska-Brzezinska, M. Electrochemical behavior of metal hydrides. *J. Solid State Electrochem.* **2001**, *5*, 229–249.
6. Ovshinsky, S.R.; Fetcenko, M.A.; Ross, J.A. Nickel metal hydride battery for electric vehicles. *Science* **1993**, *260*, 176–181.
7. Ebbesen, T.W.; Lezec, H.J.; Hiura, H.; Bennett, J.W.; Ghaemi, H.F.; Thio, T. Electrical conductivity of individual carbon nanotubes. *Nature* **1996**, *382*, 54–56.
8. Wong, E.W.; Sheehan, P.E.; Lieber, C.M. Nanobeam mechanics: Elasticity, strength, and toughness of nanorods and nanotubes. *Science* **1997**, *277*, 1971–1975.
9. Collins, P.G.; Bradley, K.; Ishigami, M.; Zettl, A. Extreme oxygen sensitivity of electronic properties of carbon nanotubes. *Science* **2000**, *287*, 1801–1804.
10. Liang, W.; Yokojima, S.; Ng, M.F.; Chen, G.; He, G. Optical properties of single-walled 4 Å carbon nanotubes. *J. Am. Chem. Soc.* **2001**, *123*, 9830–9836.
11. Minot, E.D.; Yaish, Y.; Sazonova, V.; McEuen, P.L. Determination of electron orbital magnetic moments in carbon nanotubes. *Nature* **2004**, *428*, 536–539.
12. Motta, M.; Li, Y.L.; Kinloch, I.; Windle, A. Mechanical properties of continuously spun fibers of carbon nano tubes. *Nano Lett.* **2005**, *5*, 1529–1533.
13. Psofogiannakis, G.M.; Froudakis, G.E. Study of hydrogen spill over mechanism on Pt doped graphite. *J. Phys. Chem. C* **2009**, *113*, 14908–14915.
14. Park, S.J.; Lee, S.Y. Hydrogen storage behaviors of platinum-supported multi-walled carbon nanotubes. *Int. J. Hydrog. Energy* **2010**, *35*, 13048–13054.
15. Zubizarreta, L.; Menéndez, J.A.; Pis, J.J.; Arenillas, A. Improving hydrogen storage in Ni-doped carbon nanospheres. *Int. J. Hydrog. Energy* **2009**, *34*, 3070–3076.
16. Kim, J.H.; Han, K.S. Ni nanoparticles-hollow carbon spheres hybrids for their enhanced room temperature hydrogen storage performance. *Trans. Korean Hydrog. New Energy Soc.* **2013**, *24*, 550–557.
17. Lueking, A.D.; Yang, R.T. Hydrogen spillover to enhance hydrogen storage—Study of the effect of carbon physicochemical properties. *Appl. Catal. A Gen.* **2004**, *265*, 259–268.
18. Mu, S.C.; Tang, H.L.; Qian, S.H.; Mu, P.; Yuan, R.Z. Hydrogen storage in carbon nanotubes modified by microwave plasma etching and Pd decoration. *Carbon* **2006**, *44*, 762–767.
19. Li, Z.Q.; Lu, C.J.; Xia, Z.P.; Zhou, Y.; Luo, Z. X-ray diffraction patterns of graphite and turbostratic carbon. *Carbon* **2007**, *45*, 1686–1695.
20. Okhlopkova, L.B.; Lisitsyn, A.S.; Likholobov, V.A.; Gurrath, M.; Boehm, H.P. Properties of Pt/C and Pd/C catalysts prepared by reduction with hydrogen of adsorbed metal chlorides: Influence of pore structure of the support. *Appl. Catal. A Gen.* **2000**, *204*, 229–240.
21. Arouaa, M.K.; Daud, W.M.A.W.; Yin, C.Y.; Adinata, D. Adsorption capacities of carbon dioxide, oxygen, nitrogen and methane on carbon molecular basket derived from polyethyleneimine impregnation on microporous palm shell activated carbon. *Sep. Purif. Technol.* **2008**, *62*, 609–613.
22. Arami-Niya, A.; Daud, W.M.A.W.; Mjalli, S.F.; Abnisa, F.; Shafeeyan, M.S. Production of microporous palm shell based activated carbon for methane adsorption: Modeling and optimization using response surface methodology. *Chem. Eng. Res. Des.* **2012**, *90*, 776–784.
23. Stadie, N.P.; Purewal, J.J.; Ahn, C.C.; Fultz, B. Measurements of hydrogen spillover in platinum doped super activated carbon. *Langmuir* **2010**, *26*, 15481–15485.

24. Contescu, C.I.; Benthem, K.V.; Sa, L.; Bonifacio, C.S.; Pennycook, S.J.; Jena, P.; Gallego, N.C. Single Pd atoms in activated carbon fibers and their contribution to hydrogen storage. *Carbon* **2011**, *49*, 4050–4058.
25. Ströbel, R.; Garche, J.; Moseley, P.T.; Jörissen, L.; Wolf, G. Hydrogen storage by carbon materials. *J. Power Sources* **2006**, *159*, 781–801.
26. Zubizarreta, L.; Gomez, E.I.; Arenillas, A.; Ania, C.O.; Parra, J.B.; Pis, J.J. Hydrogen storage in carbon materials. *Adsorption* **2008**, *14*, 557–566.
27. Yürüm, Y.; Taralp, A.; Veziroglu, N.T. Storage of hydrogen in nano structured carbon materials. *Int. J. Hydrog. Energy* **2009**, *34*, 3784–3798.
28. Dibandjo, P.; Zlotea, C.; Gadiou, R.; Ghimbeu, C.; Cuevas, F.; Latroche, M.; Leroy, E.; Vix-Guterl, C. Hydrogen storage in hybrid nanostructured carbon/palladium materials: Influence of particle size and surface chemistry. *Int. J. Hydrog. Energy* **2013**, *38*, 952–965.
29. Zhao, W.; Fierro, V.; Zlotea, C.; Chevalier-César, C.; Izquierdo, M.T.; Latroche, M.; Celzard, A. Carbons doped with Pd nanoparticles for hydrogen storage. *Int. J. Hydrog. Energy* **2012**, *27*, 5072–5080.
30. Midilli, A.; Ay, M.; Dincer, I.; Rosen, M.A. On hydrogen and hydrogen energy strategies: I: Current status and needs. *Renew. Sustain. Energy Rev.* **2005**, *9*, 255–271.
31. Thomas, M.K. Hydrogen adsorption and storage on porous materials. *Catal. Today* **2007**, *120*, 389–398.
32. Zlotea, C.; Cuevas, F.; Boncour, V.P.; Leroy, E.; Dibandjo, P.; Gadiou, R.; Guterl, C.V.; Latroche, M. Size-dependent hydrogen sorption in ultrasmall Pd clusters embedded in mesoporous carbon template. *J. Am. Chem. Soc.* **2010**, *132*, 7720–7729.
33. AlOthman, Z.A.; Habila, M.A.; Ali, R. Preparation of activated carbon using the copyrolysis of agricultural and municipal solid wastes at a low carbonization temperature. *Int. Conf. Biol. Environ. Chem.* **2011**, *24*, 67–72.
34. Habila, M.; Yilmaz, E.; ALOthman, Z.A.; Soylak, M. Flame atomic absorption spectrometric determination of Cd, Pb, and Cu in food samples after pre-concentration using 4-(2-thiazolylazo) resorcinol-modified activated carbon. *J. Ind. Eng. Chem.* **2014**, *20*, 3989–3993.
35. Zha, Q.F.; Hu, X.H.; Guo, Y.S.; Wu, M.B.; Li, Z.F.; Zhang, Y.Z. Improved antioxidative ability of porous carbons by boron-doping. *New Carbon Mater.* **2008**, *23*, 356–360.
36. Li, Y.; Yang, R.T. Hydrogen storage on platinum nanoparticles doped on superactivated carbon. *J. Phys. Chem. C* **2007**, *111*, 11086–11094.
37. Matsumoto, T.; Komatsu, T.; Nakanoa, H.; Arai, K.; Nagashima, Y.; Yooa, E. Efficient usage of highly dispersed Pt on carbon nano tubes for electrode catalysts of polymer electrolyte fuel cells. *Catal. Today* **2004**, *90*, 277–281.
38. Şayan, E. Ultrasound assisted preparation of activated carbon from alkaline impregnated hazelnut shell: An optimization study on removal of copper ion from aqueous solution. *Chem. Eng. J.* **2006**, *115*, 213–218.